Biochemistry

pubs.acs.org/biochemistry

Article

Distal Mutations Rewire Allosteric Networks to Control Substrate Specificity in PTP1B

Xiaoyuan Wang, Ryan M. Anderson, Jinchan Liu, Victor Batista,* and J. Patrick Loria*

Cite This: *Biochemistry* 2025, 64, 4661−4674

Read Online

ACCESS | Metrics & More | Article Recommendations | Supporting Information

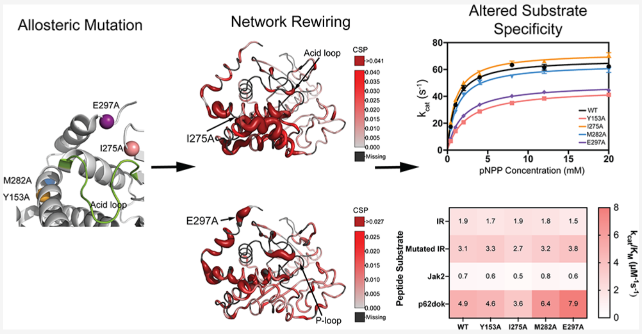

	WT	Y153A	I275A	M282A	E297A
IR	1.9	1.7	1.9	1.8	1.5
Mutated IR	3.1	3.3	2.7	3.2	3.8
Jak2	0.7	0.6	0.5	0.8	0.6
p62dok	4.9	4.6	3.6	6.4	7.9

ABSTRACT: Protein tyrosine phosphatase 1B (PTP1B) is a key regulator of cellular signaling pathways, and its dysregulation is linked to diabetes, obesity, cancer, and immune dysfunction. While the catalytic mechanism of PTP1B is conserved across protein tyrosine phosphatases, its regulation by distal allosteric sites remains less understood. Here, we investigate how mutations at four allosteric sites (Y153, I275, M282, and E297) alter the PTP1B substrate specificity and enzymatic dynamics. Kinetic analyses with phosphotyrosine peptides and *p*-nitrophenylphosphate reveal that allosteric mutants display distinct changes in catalytic efficiency (k_{cat}/K_m), in some cases reversing substrate preference relative to the wild-type enzyme. Solution NMR spectroscopy and microsecond molecular dynamics simulations demonstrate that these mutations perturb long-range communication networks, disrupting coupling between helices α3 and α7 and altering acid-loop flexibility and active-site dynamics. Notably, the E297A mutation has the most pronounced effects, rigidifying the acid loop and weakening allosteric communication to the catalytic center. Community network analysis highlights the acid loop and helix α7 as central hubs linking distal sites to the active site. Together, these results establish that distal mutations can reshape PTP1B's dynamic landscape, thereby modulating substrate specificity. This work expands our understanding of allosteric regulation in PTP1B and provides a framework for targeting dynamic networks to control phosphatase activity.

INTRODUCTION

Protein tyrosine phosphatase 1B (PTP1B, UniProtKB: P18031) is a key signaling enzyme that regulates a myriad of biochemical pathways. Dysfunction of PTP1B results in several diseases including type II diabetes, obesity, cancer, and immune system compromise.[1] Like other protein tyrosine phosphatases (PTPs), PTP1B employs a conserved catalytic mechanism (Figure 1A).[2] The reaction proceeds in two steps. First, the enzyme cleaves phosphotyrosine-containing substrates. An absolutely conserved cysteine thiolate, located in the so-called P-loop, containing the consensus sequence (I/V)-H<u>C</u>XAGXGR(S/T), nucleophilically attacks the substrate phosphorus. Simultaneously, the adjacent acid loop, which contains the conserved catalytic acid (D181), closes around the active site, positioning itself to protonate the departing phenyl group; prior works call this loop the WPD loop because the founding members of the PTP family have WPD at the N-terminus of this loop. It is now clear that most members do not have WPD in this loop, but only the catalytic acid. Therefore, we refer to this loop throughout this work as the acid loop. Phosphate cleavage releases the dephosphorylated peptide and generates a thiophosphate enzyme intermediate. In the second step, the intermediate is hydrolyzed through the coordinated actions of D181 and conserved Q262 located on the Q-loop. Substrate specificity for phosphotyrosine over phosphoserine/phosphothreonine (pSer/pTyr) arises partly from a deep active-site binding pocket formed by the pTyr loop, which contains Y46.[3]

Overall, the catalytic site is shaped by several mobile loops, including the P-, acid, Q-, pTyr, and E-loops (Figure 1B,C) whose conformational dynamics are critical for both catalysis and substrate binding.[3−7] Notably, PTP1B and other PTPs are the only known enzyme family in which a catalytic residue is located on a mobile loop. This unique feature has led to the hypothesis that regulation of catalysis may be achieved by controlling the acid-loop motion.[4] Support for this idea came from solution NMR studies, showing that the acid-loop closure kinetics closely match the time scale for substrate cleavage in related PTPs.[5]

Consistent with its role in several disease states, PTP1B has been shown to act on multiple intracellular targets.[8−11] Biochemical and structural studies indicate that PTP1B

Received: September 3, 2025
Revised: November 13, 2025
Accepted: November 17, 2025
Published: November 26, 2025

https://doi.org/10.1021/acs.biochem.5c00539
Biochemistry 2025, 64, 4661−4674

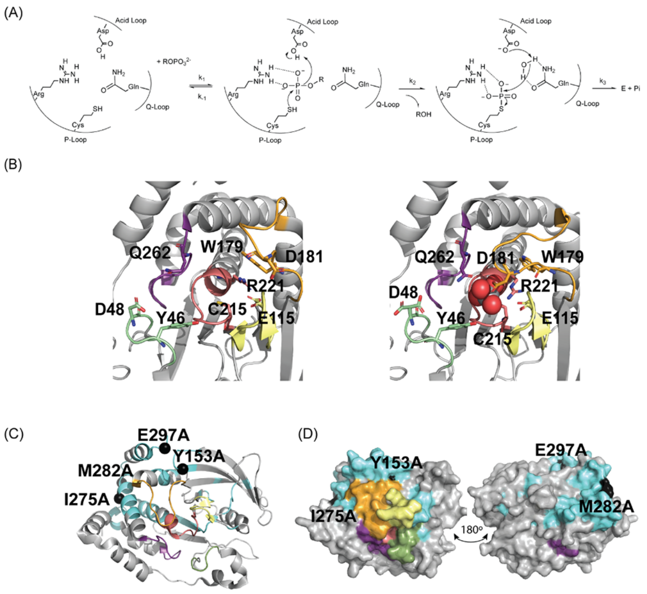

Figure 1. PTP1B mechanism and structure. (A) General mechanism of protein tyrosine phosphatases. After substrate binding (rate k_1), the nucleophilic cysteine on the P-loop attacks the phosphoester-containing substrate (k_2) to form a thiophosphate intermediate as the catalytic aspartic acid on the mobile acid loop donates a proton to the leaving group, R. In the second step, the same aspartic acid activates a water molecule coordinated by Q262 on the Q-loop to hydrolyze the intermediate (k_3). (B) The loop regions surrounding the active site are colored on a crystal structure of apo PTP1B (PDB entry 2CM2, left) and vanadate-bound PTP1B (PDB entry 3I80, right), with the catalytically important residues displayed as sticks. The coloring scheme is pTyr loop (residues 45−49) in green, E-loop (112−120) in light yellow, acid loop (177−188) in orange, P-loop (213−223) in red, and Q-loop (254−263) in violet. The left and right panels show the acid loop in the open and closed conformations, respectively. (C) The location of the loops in (B) is shown (PDB entry 1G1G) using the same coloring scheme from (B). The allosteric sites in cyan consist of $\beta3$, $\alpha2$, $\alpha4$, $\alpha6$, and $\alpha7$, and a small part of $\alpha3$ (193−197). Loops L4 (86−90), L11 (149−154), L16 (237−243), and L18 (280−285) are also shown in cyan. The same regions in panel (C) are shown in panel (D) with the same color scheme, with the sites of mutations noted in black.

preferentially dephosphorylates substrates with acidic or hydrophobic residues at the -1 position relative to the phosphotyrosine (pY) residue (with "−" indicating N-terminal to the pY residue, whereas "+" indicates amino acids just C-terminal to the pY group).[12,13] It has been suggested that PTP1B favors Met at the +1 position, with weaker preference for Gln and Ser, while disfavoring substrates with positively charged residues N-terminal to pY or with Gly/Pro flanking the pY site.[13] *In vivo*, PTP1B has been shown to dephosphorylate the insulin receptor (IR),[14] Janus kinase 2 (Jak2),[15] p62$^{\text{dok}}$,[11] and the epidermal growth factor receptor (EGFR),[8] among others.[16] Complementary *in vitro* screening studies have identified a broad range of substrate diversity for pY peptides cleaved by PTP1B.[17,18] This broad substrate specificity implies that PTP1B activity is subject to multiple layers of regulation within the cells. Reported mechanisms include reversible oxidation,[19,20] post-translational modification,[21−24] and subcellular localization.[25,26] In addition, PTP1B harbors allosteric sites, although their physiological roles remain poorly understood. While there is limited detail on *in vivo* allostery of PTP1B, we wondered if perhaps allosteric sites on PTP1B could alter its substrate specificity. One such allosteric site, located between $\alpha3$ and $\alpha6$, was identified in an inhibitor screen.[27] Ligand binding at this site restricted the closure of the acid loop and limited catalytic activation. Subsequent studies have revealed and characterized additional allosteric sites in PTP1B.[28−34]

Building on our previous work, which identified multiple distal sites of PTP1B where mutation perturbs catalytic activity (Figure 1D),[34,35] we sought to determine how these mutations influence substrate specificity, protein structure, and enzyme dynamics. Here, we combine experimental and computational approaches to explore how allosteric mutations trigger cascades of altered long-range interactions that rewire conformational dynamics on nanosecond to millisecond timescales. These dynamic changes remodel the native active site environment, ultimately reshaping the conformational ensemble of catalytic residues and substrate-binding determinants.

■ MATERIALS AND METHODS

Site-Directed Mutagenesis. Site-directed mutagenesis was performed using the QuickChange Site-Directed Mutagenesis Kit using primers listed in SI Table 1. The correct DNA plasmid sequence was confirmed by DNA sequencing at the Keck DNA Sequencing Core (Yale University).

Protein Expression and Purification. The expression plasmids containing the gene for the WT and mutant PTP1B were transformed into BL21(DE3) cells. For kinetics experiments, *E. coli* were grown in 50 mL of LB broth with 50 μg/mL kanamycin at 37 °C overnight and transferred to 1 L of LB with 50 μg/mL kanamycin and grown at 37 °C. Protein induction was achieved with 0.5 mM IPTG when the OD$_{600}$ of the cell culture reached a value of 1.0, and expression was continued at 25 °C for 18 h, at which time the cells were harvested by centrifugation at 4 °C and 7400*g* for 45 min.

For NMR studies, *E. coli* were grown in 5 mL of H_2O LB at 37 °C overnight. After this initial growth culture, 2 mL of the LB starting culture was centrifuged at 3000*g* for 5 min at room temperature, and the pellet was resuspended in 20 mL of LB prepared using recycled D_2O (typically ∼90% ^{2}H content). After 8 h of growth at 37 °C, the D_2O LB culture was centrifuged at 3000*g* for 10 min at room temperature, and the pellet was resuspended in 100 mL of 2× M9 minimal medium prepared with recycled D_2O and grown at 37 °C overnight and subsequently was centrifuged for 10 min at 3000*g* at room temperature. The resulting cell pellet was resuspended in 1 L of 2× M9 minimal medium prepared with 99.9% D_2O, 1 g of $^{15}NH_4Cl$, and 2 g of glucose/dextrose and grown until the OD$_{600}$ reached ca. 0.8. Half an hour before induction, 60 mg/mL α-ketobutyric acid and 100 mg/mL α-ketoisovaleric acid (Cambridge Isotope Laboratories) were added for the ^{13}C labeling of methyl groups of isoleucine, leucine, and valine (ILV). The cells were then induced with 0.5 mM IPTG, and induction was continued for 18 h before the cells were harvested at 4 °C and 7400*g* for 45 min.

PTP1B Purification. The cell pellet was resuspended in 5 mL of lysis buffer (50 mM Tris, 500 mM NaCl, and 5% glycerol, pH 8.0 for each 1 g of pellet). One tablet of cOmplete Mini EDTA-free protease inhibitor was also added, and the cells were then lysed by sonication on ice. The cell lysate was centrifuged for 45 min at 4 °C at 27000*g*, and the supernatant was filtered through a 0.45 μm filter and loaded to a nickel column. The column was washed with 12 CV of wash buffer (50 mM Tris, 500 mM NaCl, 20 mM imidazole, 5% glycerol), and the protein was eluted with 12 mL of elution buffer (50 mM Tris, 500 mM NaCl, 300 mM imidazole, 5% glycerol). Fractions containing the His-tagged PTP1B were pooled, and the affinity tag was removed with TEV protease under dialysis in 50 mM Tris, 500 mM NaCl, 20% glycerol, and 0.5 mM 2-mercaptoethanol, pH 8.0, at 4 °C with a PTP1B:TEV concentration ratio of ca. 3:1. The resulting mixture was loaded onto the nickel column again, and the cleaved PTP1B was then collected from the flow-through while the His tagged TEV was retained on the column. PTP1B-containing fractions were pooled and concentrated using an Amicon concentrator at 4 °C. Typically, ^{13}C-ILV-labeled samples were then immediately used in NMR experiments.

Presteady-State (Stopped-Flow) Kinetics. Purified PTP1B (1−301) was dialyzed in 50 mM Tris, 50 mM Bis-Tris, 100 mM sodium acetate, pH 6.0 and concentrated to 120−260 μM. Presteady-state kinetics experiments were performed using 20 mM *p*-nitrophenylphosphate (pNPP) as the substrate at 3.5 °C to resolve the initial burst phase on an Applied Photophysics SX40 instrument. The change in absorbance was measured at 410 nm for 200 ms and quantified using a pNP extinction coefficient of 1846 $\mathrm{cm^{-1}\ M^{-1}}$. A total of 4000 points were collected for a single run. Specifically, two separate syringes with 120−260 μM of enzyme and 40 mM of pNPP were installed onto the instrument. The final concentration of enzyme and pNPP in the reaction chamber ranged from 60 to 130 μM and 20 mM, respectively.

The kinetic rate constants when $[S] \gg [E]$ were extracted by fitting the average of five runs to the exponential equation as described previously.[36] The absorbance was transformed and normalized by dividing the absorbance by the concentration of the enzyme and the extinction coefficient of pNP. Briefly, for the PTP reaction scheme in Figure 1A, R is the *p*-nitrophenyl group. For burst kinetics observed for PTP1B, the rapid increase in absorbance due to the time-dependent increase in [*p*-nitrophenolate] upon cleavage and hydrolysis of the phosphate group is modeled as

$$[p\text{-nitrophenolate}] = At + B(1 - \mathrm{e}^{-bt}) + C \tag{1}$$

In eq 1, t = time in seconds, $b = (k_2 + k_3)$ and the linear portion, $A = k_2k_3/(k_2 + k_3)$, and B is the amplitude of the burst. Thus, fitting of the stopped-flow data yields forward chemical rate constants for both cleavage (k_2) and hydrolysis (k_3). Stopped-flow data was fit with the Kintec Explorer software package.

Steady-State Kinetics with pNPP. All steady-state pNPP kinetic experiments were performed at 30 °C in 50 mM Tris, 50 mM Bis-Tris, and 100 mM sodium acetate, pH 6.0, in triplicate. Initially, 100 nM of PTP1B was added to buffered solutions containing 0.4, 1.0, 2.0, 4.0, 8.0, 12.0, and 20.0 mM of pNPP. After 10, 20, 30, and 40 s, a 200 μL aliquot of this mixture was added to 800 μL of 1.0 M NaOH to quench the reaction. The absorbance at each time point was measured at 405 nm and converted to concentrations using an extinction coefficient of 18000 $\mathrm{cm^{-1}\ M^{-1}}$. The linear portion of this fixed time point assay was used to construct the initial rates, which were combined with [S] and the data were fit with the Michaelis−Menten expression in Prism v10 (GraphPad).

Steady-State Kinetics with Peptides. Phosphorylated peptide substrates were purchased from Lifetein and Genescript in HPLC-purified form at 95% purity and were used without further purification. Peptide cleavage/hydrolysis reactions were monitored continuously at 282 nm, which shows an absorbance for tyrosine when pY is dephosphorylated.[37] For the peptide stock solution, Insulin Receptor (IR) peptide (sequence Ac-TDpYYRKG-$\mathrm{NH_2}$), mutated IR peptide (sequence Ac-TDpYYRAG-$\mathrm{NH_2}$), Janus kinase2 (Jak2) peptide (sequence Ac-KEpYYKVK-$\mathrm{NH_2}$), and p62$^{\mathrm{dok}}$ peptide (sequence Ac-TALpYSQVQ-$\mathrm{NH_2}$) were dissolved in 50 mM Tris, 50 mM Bis-Tris, and 100 mM sodium acetate at pH values of 6.0, 7.0, 6.0, and 5.0, respectively, to prevent aggregation. For each peptide, pY is the location of the phosphotyrosine group, and Ac ($\mathrm{NH_2}$) are acetyl (amino) groups. The reaction solution was prepared by adding an appropriate amount of the stock solution to the kinetics buffer (50 mM Tris, 50 mM Bis-Tris, 100 mM sodium acetate, pH 6.0) so that the final peptide concentration was 30−130 μM for IR, 30−100 μM for mutated IR, 50−350 μM for Jak2, and 40−150 μM for p62$^{\mathrm{dok}}$. The pH in the final reaction was 6.0. To initiate the reaction, 25 nM of PTP1B was added to the buffered peptide solution at 30 °C, and the absorbance was monitored continuously every 0.2 s at 282 nm. The reaction was performed in triplicate at four different substrate concentrations. The entire progress curves for all [S] were globally fit with Prism version 10 using the Lambert function[38,39] approximation of the integrated rate expression eq 2

$$P = S - K_{\mathrm{m}}\cdot\ln 1.2\frac{\frac{S}{K_{\mathrm{m}}}\mathrm{e}^{x}}{\ln 2.4\left(\frac{S}{K_{\mathrm{m}}}\mathrm{e}^{x}\right)\ln\left(1 + 2.4\cdot\frac{S}{K_{\mathrm{m}}}\mathrm{e}^{x}\right)} + \text{offset} \tag{2}$$

to obtain k_{cat} and K_{m} values.

The four optimal concentrations of peptides used above were determined by first estimating the kinetic constants in trial experiments with 50 and 100 μM peptides and 25 nM WT enzyme, followed by fitting the progress curves to obtain initial k_{cat} and K_{m}. A Monte Carlo simulation was then performed with the estimated k_{cat} and K_{m} including 5% random uncertainty, to determine the optimal values of [S] to use.

NMR Experiments. ^{1}H−^{15}N TROSY and ^{1}H−^{13}C methyl TROSY 2D spectra for WT and mutant PTP1B were acquired at 14.1 T. ^{15}N spectra were acquired with 3412 (1706) t_1 (t_2) points with spectral widths of 10000 (2500) Hz, respectively. ^{13}C spectra were acquired with 3778 (1889) t_1 (t_2) points with spectral widths of 8503 (3200) Hz, respectively. All NMR experiments were conducted at 19 °C as calibrated with a methanol standard and at pH 6.8. ^{13}C methyl multiple quantum relaxation dispersion experiments[40] were conducted at 16.5 T with 3778 (1889) t_1 (t_2) points, spectral widths of 8503 (4400) Hz, carbon carrier frequency at 19.5 ppm, using a 20 ms constant time relaxation period, with τ_{cp} values of 0.41667, 0.5, 0.45455, 0.625, 0.55556, 0.7143, 1, 1.25, 1.66667, 2.5, and 5 ms. Relaxation data were fit using Chemex (Reference Bouvignies, G. Gbouvignies/ChemEx, 2025. https://github.com/gbouvignies/ChemEx). Amide (^{1}H/^{15}N) chemical shifts were taken from the BioMagResBank (accession #5474)[41] and methyl (^{1}H/^{13}C) ILV chemical shift assignments were obtained from Torgeson et al.[42] and from Cui et al.[35]

MD Simulations. All molecular dynamics (MD) systems were constructed based on the 1.95 Å crystal structure of human PTP1B (PDB ID: 1SUG), comprising residues 1−301. Three systems were prepared: wild-type (WT), E297A, and I275A. Each system was modeled using psfgen and solvated in

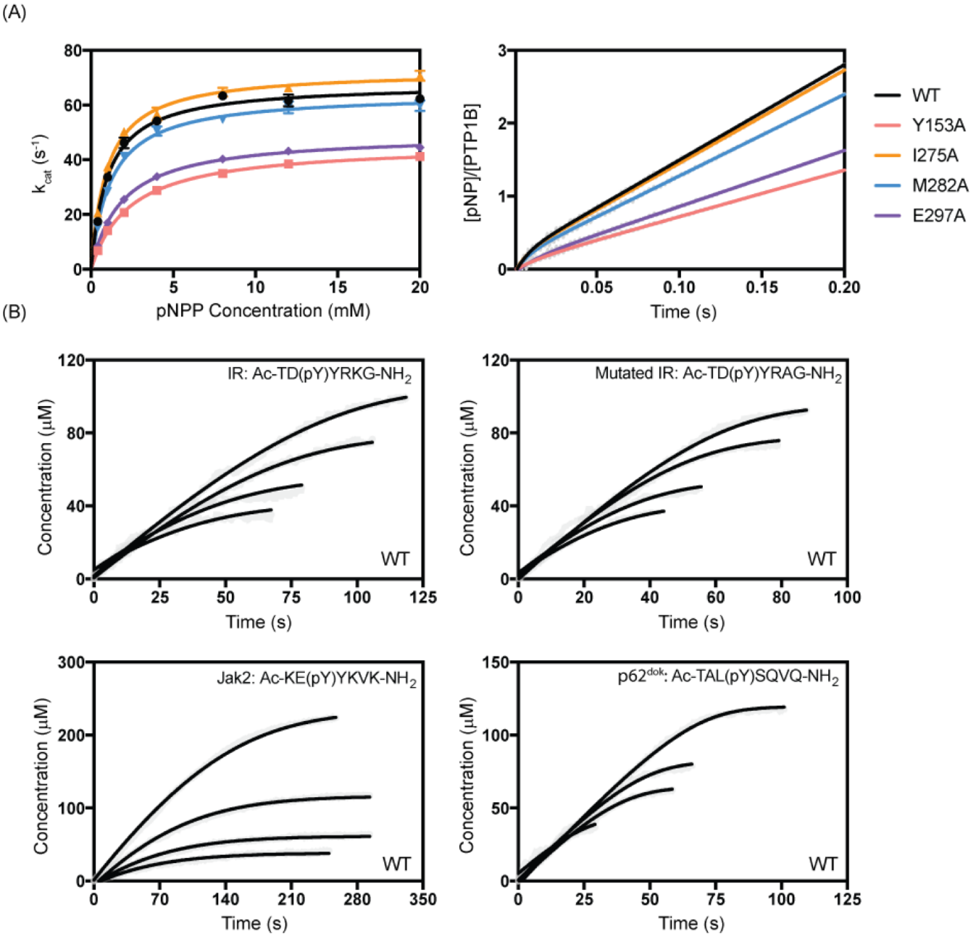

Figure 2. Steady-state and presteady-state kinetics of PTP1B. (A) Steady-state (left) and stopped-flow (right) experiments were performed for WT and allosteric mutants with pNPP as the substrate. (B) Progress curves representing the formation of dephosphorylated peptides as a function of time with WT PTP1B. Black lines are the nonlinear least-squares fit to the gray data points. The peptide sequences are shown at the top of each panel. Identical experiments for the mutants are shown in the Supporting Information.

a cubic box of TIP3P water (90 × 90 × 90 Å^3),[43] with 0.15 M NaCl added to mimic physiological ionic strength and ensure system neutrality.

Simulations were performed in NAMD[44] using the CHARMM36m[45] force field for proteins. Each system underwent a three-stage equilibration protocol: (1) 1 ns with water and ions relaxed while restraining protein atoms, (2) 5 ns with side chains and solvent relaxed while the backbone was restrained, and (3) 5 ns with all atoms unrestrained. Production trajectories were run for 200 ns × 8 replicas per system.

The temperature was maintained at 310 K using Langevin dynamics (damping coefficient $\gamma = 1.0$ ps^{-1}), and pressure was controlled at 1 atm using an anisotropic Langevin piston barostat.[46] Simulations used a 2 fs integration time step. Bonded and nonbonded interactions were computed at every step. Lennard-Jones interactions used a 12 Å cutoff with a switching function applied from 10 to 12 Å. Electrostatics were evaluated using the particle mesh Ewald method,[47] in which pairwise interactions were computed directly within 12 Å, and interactions beyond this distance were calculated on the Ewald mesh, updated every other step.

MD trajectories were analyzed using VMD,[48] MDiGest,[49] and MDAnalysis.[50,51] All RMSF, correlation, and community calculations were performed on Cα atoms for each residue. Per-residue RMSF values for each simulation were computed for Cα atoms using VMD and were averaged over eight replicas for analysis. RMSF percent differences from WT and CSP data were mapped onto the protein structure using MDAnalysis and were visualized using Pymol.[52]

Pairwise correlations and eigenvector centralities[53] were computed using the generalized correlation coefficients[54] derived from mutual information[55] using default parameters as implemented in MDiGest. The resulting correlation matrices and eigenvector centralities were each averaged over eight replicas for each protein for analysis.

Communities were generated from the averaged correlation and distance matrices using the Louvain heuristic scheme[56] with 20 iterations, as implemented in MDiGest. Communities smaller than five residues were redistributed to maximize modularity, as implemented in MDiGest. Community structure visualizations and the corresponding eigenvector centrality plots were generated using MDiGest, Pymol, and Matplotlib.[57]

Distance and dihedral measurements were performed by using MDAnalysis. For residues with multiple equivalent atoms, the center of mass of those atoms was used to calculate distances. The corresponding histograms for each protein were generated using pandas,[58] NumPy,[59] and Matplotlib using all measurements from the eight replicas. Bin sizes of 0.1 Å and 3.6° were used for distance and dihedral histograms, respectively.

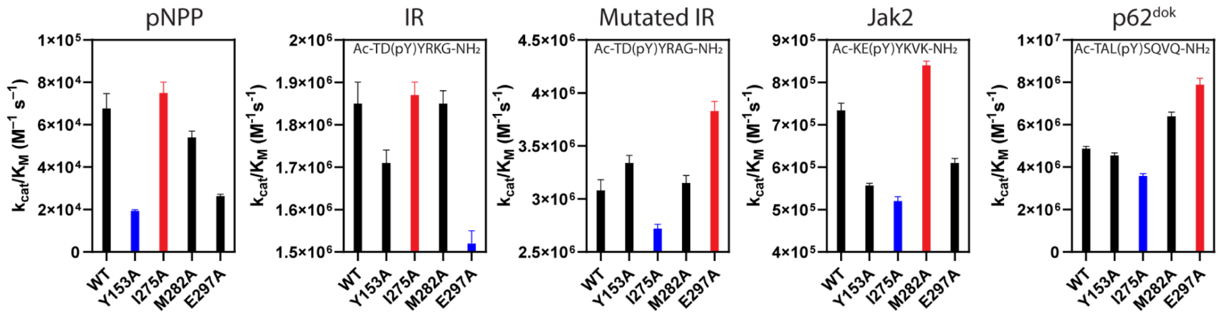

Figure 3. Bar graph representation of the catalytic efficiency of k_{cat}/K_m with different PTP1B peptides and pNPP substrates. The substrate is indicated at the top of each panel, and the highest (lowest) k_{cat}/K_m values are indicated in red (blue). The mutant PTP1B enzyme is indicated at the bottom of each panel.

RESULTS AND DISCUSSION

Allosteric Mutants Alter PTP1B−Substrate Interactions. We generated single alanine point mutants of PTP1B at positions I275, M282, E297, and Y153, previously identified as residues that influence catalytic turnover.[34] The locations of these mutations are shown in Figure 1D. All are distal from the nucleophilic C215 in the P-loop, with distances of 30 Å (M282), 23 Å (I275), 21 Å (E297), and 15 Å (Y153). Each mutant was expressed successfully and retained its catalytic activity.

Kinetic parameters for phosphotyrosine-containing peptides were determined by global fitting of full progress curves at multiple substrate concentrations, monitoring absorbance changes at 282 nm.[37] For the small-molecule substrate *p*-nitrophenylphosphate (pNPP), parameters were obtained from linear-rate profiles using standard Michaelis−Menten analysis. The results are summarized in Figures 2, 3 and SI Figures 1 and 2.

Specificity constants (k_{cat}/K_m) for peptide substrates ranged from 5 × 10^5 M^{-1} s^{-1} to 8 × 10^6 M^{-1} s^{-1}, consistent with previously reported values for PTP1B.[37] However, the k_{cat}/K_m values vary substantially among mutants and substrates, in some cases switching the relative order of substrate specificity. For example, for the IR peptide, I275A displayed the highest k_{cat}/K_m, while E297A was the lowest. In contrast, with the p62^{dok} peptide, E297A had the highest k_{cat}/K_m and I275A had the lowest. Overall, WT PTP1B generally exhibited the highest k_{cat} values for peptide substrates, with the exception of the IR variant peptide (SI Figures 1 and 2). For pNPP, WT showed a lower k_{cat} than I275A but higher than those of the other mutants. Notably, in most mutants, reduced K_m values compensated for lower turnover numbers, resulting in elevated k_{cat}/K_m values relative to those of the WT (Figure 3, SI Figure 2). These steady-state data demonstrate that allosteric mutations differentially affect kinetic constants across substrates, indicating that distal sites can rewire PTP1B substrate specificity.

The E297A mutant shows the largest deviations in k_{cat}/K_m values relative to those of WT, with the exception of the Jak2 substrate (SI Figure 2). Specifically, k_{cat}/K_m values for E297A differ from those of WT by −18%, + 61%, +24%, and −14% for the IR, p62^{dok}, mutant IR, and Jak2 substrates, respectively. Y153A and I275A also exhibit deviations from WT, though to a lesser extent than E297A, with both increases and decreases observed depending on the substrate. In contrast, M282A consistently yields higher k_{cat}/K_m values than WT, ranging from only 0.2% above that of WT for the IR substrate to 31% above for p62^{dok}. Collectively, these data indicate that substrate-dependent differences in k_{cat}/K_m between the WT and mutants are substantial. Notably, the kinetic trend observed with the small-molecule substrate pNPP diverges from those of the peptide substrates. Given this distinction, we examined presteady-state kinetics of WT and mutant enzymes using pNPP as the substrate (Figure 2A).

At 3.5 °C, presteady-state analysis yielded k_2 (cleavage) and k_3 (hydrolysis) values of 120 ± 6 s^{-1} and 15.0 ± 0.1 s^{-1} for WT, 124 ± 4 s^{-1} and 12.1 ± 0.1 s^{-1} for I275A, and 111 ± 5 s^{-1} and 11.8 ± 0.1 s^{-1} for M282A. The close agreement among these values indicates that I275A and M282A have minimal effects on the individual cleavage and hydrolysis steps for pNPP. This conclusion is consistent with steady-state kinetic measurements at 30 °C, where pNPP k_{cat} values were 68 ± 2 s^{-1} (WT), 73 ± 1 s^{-1} (I275A), and 65 ± 1 s^{-1} (M282A). Similarly, the K_m values for I275A (1.0 ± 0.1 mM) and M282A (1.2 ± 0.1 mM) were comparable to those of WT (1.0 ± 0.1 mM).

In contrast, mutations Y153A and E297A in the allosteric region (Figure 1C,D)[34] produced pronounced reductions in catalytic efficiency. Both mutants exhibited approximately 2-fold decreases in k_2 (62 ± 3 s^{-1} for Y153A; 71 ± 7 s^{-1} for E297A) and in k_3 (7.0 ± 0.04 s^{-1} for Y153A; 8.6 ± 0.1 s^{-1} for E297A), along with a 2-fold increase in K_m (2.4 ± 0.1 mM for Y153A; 2.0 ± 0.1 mM for E297A).

Taken together, these experiments demonstrate that the allosteric mutants not only alter the individual rate constants for pNPP relative to those of WT but also modulate substrate specificity (k_{cat}/K_m) across different peptide substrates. This suggests that the allosteric sites play a direct role in regulating PTP1B−peptide interactions. To further elucidate the connection between the allosteric and active sites, we employed solution NMR spectroscopy in combination with μs-timescale molecular dynamics (MD) simulations. For the remainder of this work, we focus on E297A, which exhibits the most pronounced deviations from WT, and I275A, which behaves similarly to WT with the IR peptide but diverges with the other substrates.

Allosteric Mutations Have Distinct Effects across the PTP1B Structure. We mapped the effects of allosteric mutations on the active site and substrate-binding pocket by using solution NMR spectroscopy and μs-MD simulations. Specifically, we combined NMR chemical-shift perturbation (CSP) analysis, NMR relaxation experiments, and differential root-mean-square fluctuations (ΔRMSF) analysis of the protein backbone from MD simulations (Figure 4).

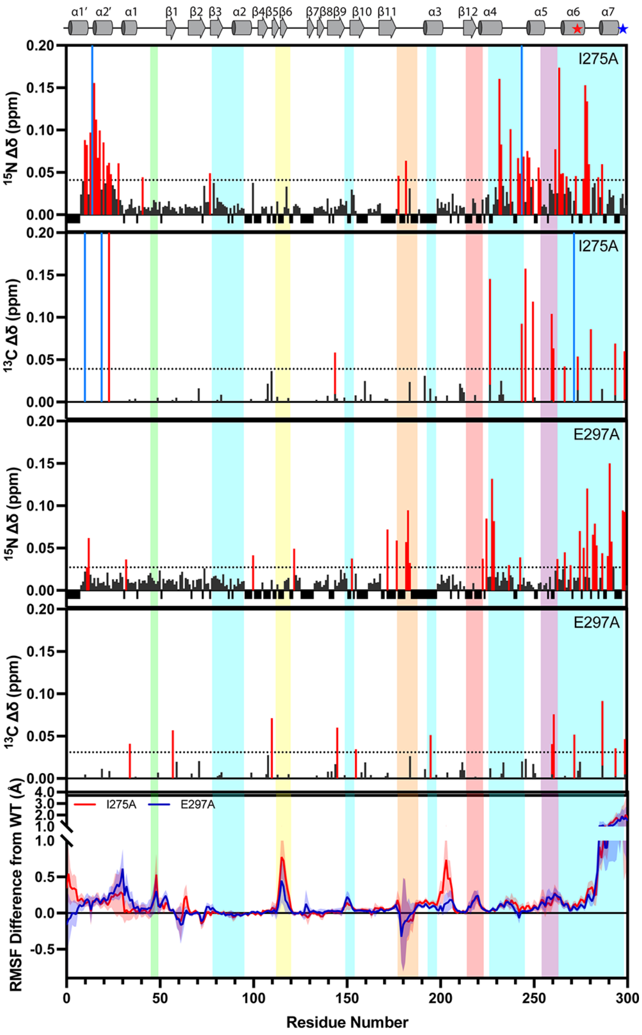

Figure 4. NMR and MD comparisons between PTP1B enzymes. ^{15}N(amide), ^{13}C (ILV) NMR chemical shift perturbations (CSP) between apo WT and apo I275A/E297A, and the root-mean-square-fluctuation differences obtained from MD simulation are shown in the bottom panel. The differences are shown as a function of the amino acid residue number. For the CSP plots, prolines and unobserved and overlapped residues are shown as negative black tics. Amino acid residues whose chemical shifts change significantly, making their assignments ambiguous, are indicated as blue bars. That these residues' chemical shifts move significantly indicates they are impacted by the mutation; therefore, we color them differently from the other residues. Residues with a CSP above the 1.5 standard deviation over the 10% trimmed mean (horizontal black dotted line) are colored in red. The RMSF difference was obtained by subtracting the average WT RMSF from the mutant's. Errors were computed for each residue using the standard error of the mean over eight replicas and are indicated with shaded regions surrounding the data points. Data representing I275A and E297A are colored red and blue, respectively. The PTP1B secondary structure is indicated at the top of the figure, and loop regions are indicated with colored bars as in Figure 1B,C. The locations of the I275A and E297A mutants are shown as red and blue stars, respectively.

The NMR experiments probed both the amide backbone using ^{15}N-based experiments and the hydrophobic side chains using ^{13}C-based experiments targeting the methyl groups of isoleucine, leucine, and valine (ILV). CSP values, calculated as the differences between WT PTP1B and the I275A and E297A mutants, are shown in Figure 4. Statistically significant CSPs are highlighted as red bars and mapped onto the three-dimensional structure of PTP1B (Figure 5). While I275A and E297A share some similarities in their CSP profiles, they also display distinct and mutation-specific differences.

For the I275A mutant, significant chemical shift changes are observed at the N-terminal helices $\alpha1'$ and $\alpha2'$ (residues 1−30), within the acid loop, and extensively throughout the C-terminal region beyond $\alpha4$, including the Q-loop, $\alpha6$, and $\alpha7$. Additional perturbations are detected at K41, A77, L144, T178, and F182. Importantly, differences in chemical shifts in acid loop residues T178 and F182 indicate that this mutation alters the chemical environment of this remote, catalytically essential element. The strong perturbations at the N-terminus are consistent with structural packing interactions, as the I275 Cδ atom lies within 3.0 and 3.3 Å from the γ and β carbons of M3 and E4, respectively.

Complementarity between the NMR and MD techniques is evident in this mutant. Both approaches reveal altered dynamics at the N-terminal region, $\alpha6$ and $\alpha7$, as well as the acid loop (Figures 4 and 5). However, MD simulations additionally capture deviations between I275A and WT not apparent by NMR, particularly in the E-loop, pTyr loop, Q-loop, and P-loop. Notably, the P-loop is typically rigid in both NMR and computational studies of the WT enzyme,[60] suggesting that the I275 mutation perturbs multiple aspects of the active site structure and dynamics beyond local packing interactions.

The E297A mutant exhibits more extensive chemical shift perturbations in $\alpha7$ than in I275A, consistent with the location of E297 within this helix. In contrast, $\alpha5$ shows fewer perturbed residues in E297A than in I275A. Both mutants display CSP in the acid loop (T177, F182, G183, and V184) and Q-loop (L260, I261, and T263). Simulations suggest that each mutation induces rigidification of the acid loop on the fast time scale (Figures 4 and 5). However, the pTyr recognition loop residues in E297A exhibit a smaller increase in RMSF relative to WT.

At the structural level, E297A disrupts a hydrogen bond linking $\alpha7$ and $\alpha3$ by eliminating the interaction between the E297 side-chain O$^{\varepsilon}$ and the N193 side-chain atom, N$^{\delta2}$ (Figure 6A,E). By comparison, I275A perturbs packing between $\alpha6$ and the N-terminal helices $\alpha1'$ and $\alpha2'$ (Figure 6D); distance distributions for molecular interactions in this region are significantly broadened and shifted toward shorter distances for I275A (SI Figure 3). Consistent with these computational results, NMR relaxation dispersion experiments reveal changes near $\alpha3$ at L195 in both mutants (Figure 6B). E297A further produces unique dynamic effects in $\alpha7$. Relaxation dispersion and R_2 analyses show marked perturbations for L294 and V287, with residues involved in hydrophobic packing within the $\alpha7$ C-terminus (Figure 6C and SI Figure 5). Specifically, the V287 ^{13}C$^{\gamma1}$(^{13}C$^{\gamma2}$) R_2 values for WT PTP1B are 52.2 ± 0.6 s^{-1} (65.5 ± 1.2 s^{-1}), whereas in E297A and I275A, these rates are, respectively, 25.9 ± 0.1 s^{-1} (34.9 ± 0.5 s^{-1}) and 43.4 ± 0.5 s^{-1} (unassigned in I275A). Likewise, for L294, the ^{13}C$^{\delta1}$(^{13}C$^{\delta2}$) R_2 values for WT, E297A, and I275A are 12.9 ± 0.04 s^{-1} (24.9 ± 0.1 s^{-1}), 15.1 ± 0.02 s^{-1} (15.6 ± 0.03 s^{-1}), and 14.0 ± 0.05 s^{-1} (23.2 ± 0.2 s^{-1}), respectively. These data confirm that both mutations perturb the dynamics of $\alpha7$, with E297A exerting the stronger effect, as shown by the R_2 values (SI Table 3).

Notably, residues L294 and V287, as well as helix $\alpha7$ more broadly, have been shown to rigidify upon binding of the active-site inhibitor TCS-401.[42] Previous studies also estab-

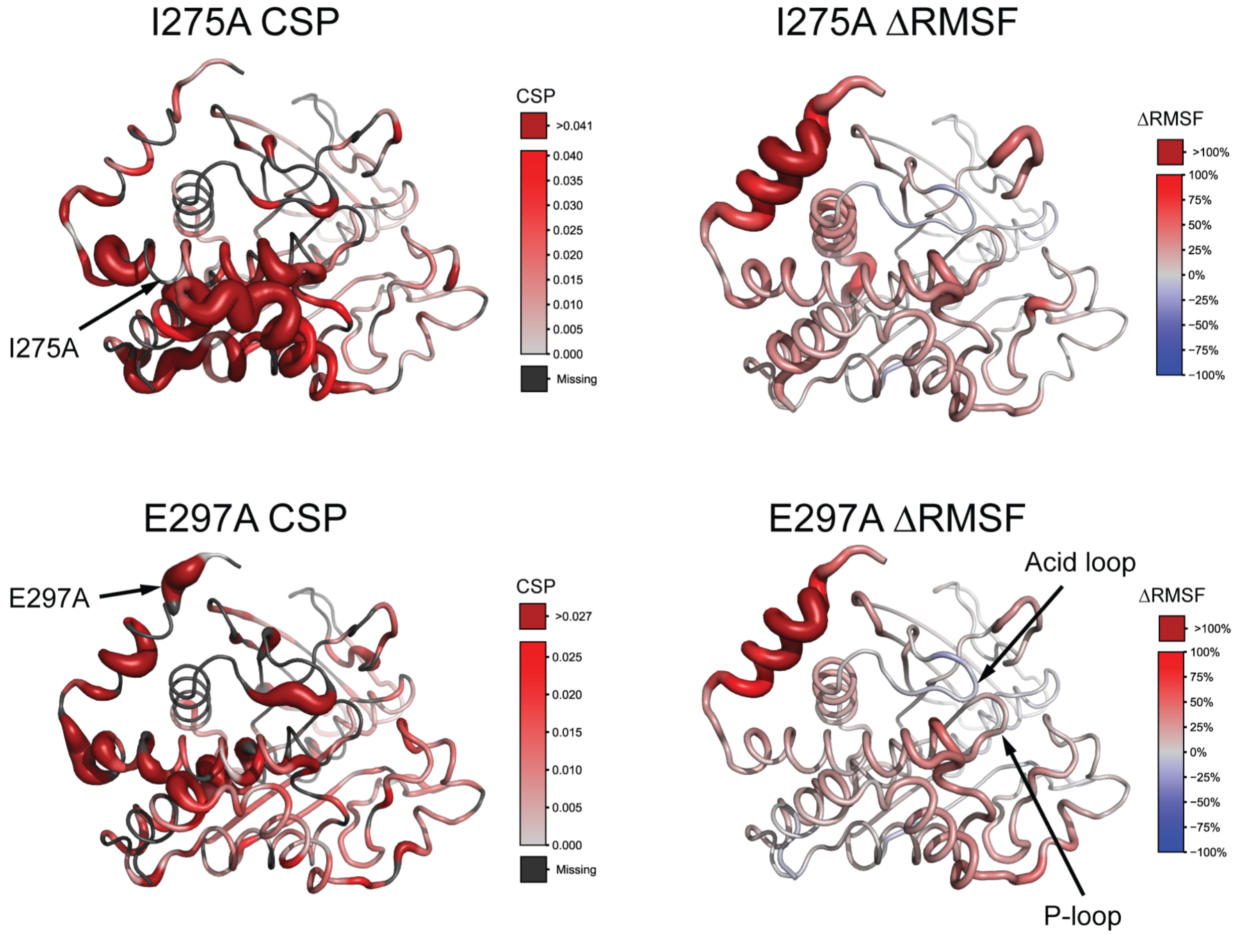

Figure 5. Mutation-induced changes in PTP1B. (Left) Amide CSP values from Figure 4 are plotted onto the crystal structure of PTP1B. The magnitude of the CSP difference is depicted with a gray-to-red color change and an increase in the radius of the backbone sausage. Residues exhibiting significant amide CSP above 1.5 standard deviations over the trimmed mean are colored in dark red. (Right) PTP1B root-mean-square-fluctuation percent differences (ΔRMSF) from WT are plotted onto the crystal structure, with the blue-to-red color gradient indicating more rigid than WT to more flexible than WT, respectively. The increase in radius also represents the size of the ΔRMSF values by percentage. Residues that are overlapped, not observable, or unassigned are indicated in black. The P-loop, acid loop, and site of mutation are noted with arrows.

lished the role of α7 in PTP1B allosteric communication, whereby active-site ligand binding stabilizes the C-terminus and dampens conformational exchange throughout PTP1B.[42] Together, these findings reinforce the central role of α7 as a conduit linking distal mutations and allosteric regulation to the catalytic core.

Previous computational studies of WT PTP1B identified W291 in α7 as a structural anchor within the hydrophobic pocket formed by F280 and A189.[61] Disruption of this region in the E297A mutant strengthens the interaction between W291 and F280, as observed in MD simulations, while simultaneously increasing the distance between W291 and A189, which lies in the C-terminal region of the acid loop (SI Figure 4A). This altered packing is accompanied by decreased $^{13}CH_3$ R_2 values for I281 (Figure 7, SI Table 3) and by substantial changes in the χ1 and χ2 dihedral angle distributions of W291, indicating conformational rearrangements of this aromatic side chain (SI Figure 4B).

Other residues within this hydrophobic cluster, including L192, L195, and L272, also show significant reductions in R_2 values in both I275A and E297A compared to those in WT (SI Table 3). Notably, these residues are located near the allosterically critical "197" site identified by Keedy et al.[29] and L192 independently identified in computational work by Kamerlin and coworkers, as part of a core allosteric communication network that governs PTP1B catalytic activity.[60] Collectively, our data reinforce these findings, showing that perturbations in α7 propagate through this conserved residue network, ultimately relaying allosteric effects to the active site.

The altered interaction between A189 and W291 is particularly notable, as A189 resides at the C-terminus of the acid loop. Additional perturbations are observed in this region, including changes to contacts between S187 and residues 190 and 191, which cap α3 and serve as a hinge point for acid-loop motion (SI Figure 4C).[31]

Both I275A and E297A mutants exhibit reduced ^{13}C R_2 values for residues near the acid loop compared to those of WT, with the strongest effect in E297A. For example, the $^{13}C^{\delta1(\delta2)}$ R_2 values of L110 decrease by 28 s^{-1} (36 s^{-1}) in E297A relative to WT values of 63.3 ± 1.5 s^{-1} (75.5 ± 3.6 s^{-1}) (SI Table 3). In contrast, the reductions in I275A are more modest (9 and 8 s^{-1}). L110 resides in the E-loop, which has been shown by MD simulations to exhibit coordinated motions with the P-loop in the active site and aids in acid-loop closure.[60] Residue L110 lies in close proximity to the active site—5 Å from the catalytic C215 and 6 Å from the N-terminal hinge of the acid loop—positioning it as a key

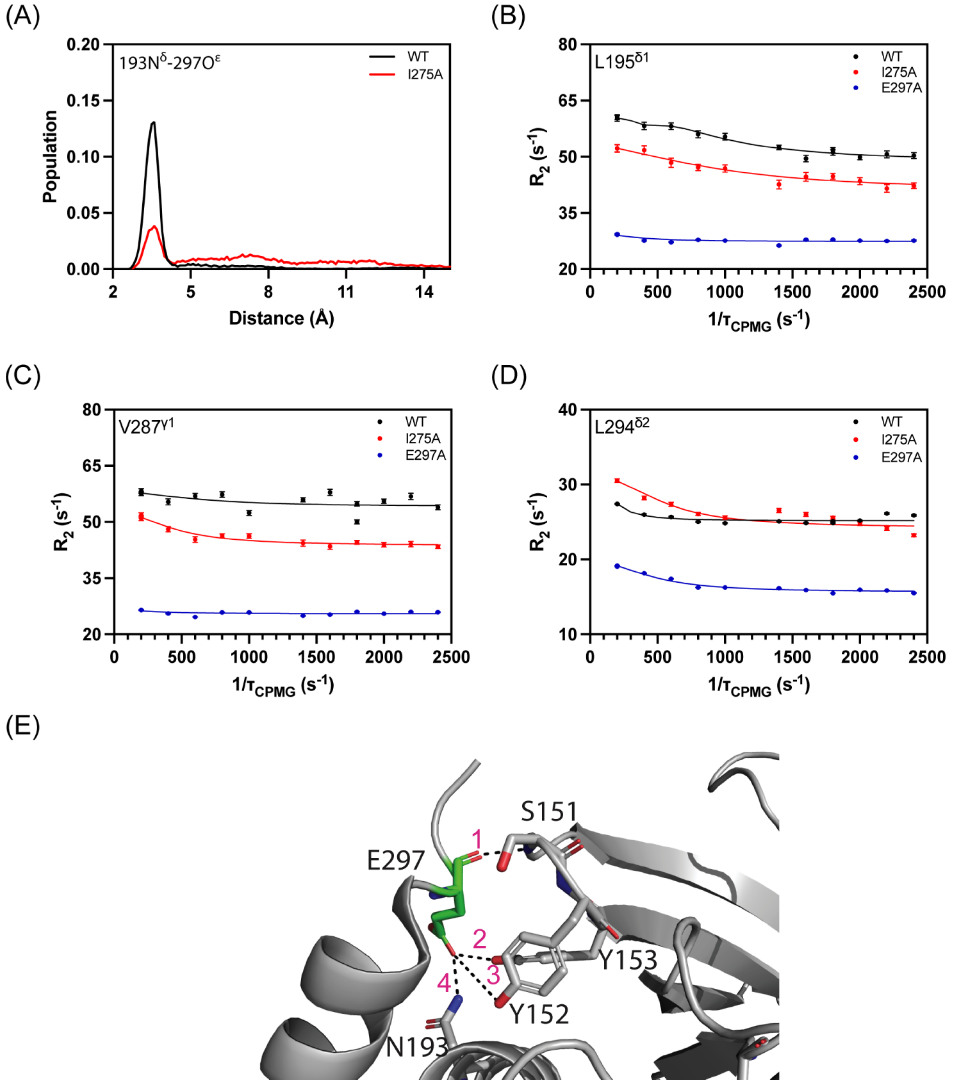

Figure 6. $\alpha 3$ and $\alpha 7$ helices are connected by a hydrogen bond network. (A) The distance profile from MD simulations between O^{ε} of the E297 side chain and the $N^{\delta 2}$ side chain of N193. Carr−Purcell−Meiboom−Gill relaxation dispersion of apo PTP1B collected at 800 MHz with a total relaxation time of 20 ms showed (B) L195$^{\delta 1}$, (C) V287$^{\gamma 1}$, and (D) L294$^{\delta 2}$. (E) Snapshot from the MD simulation showing that E297 interacts with (**1**) S151, (**2**) Y153, and (**3**) Y152 in L11 and (**4**) N193 in $\alpha 3$, indicated by dotted lines.

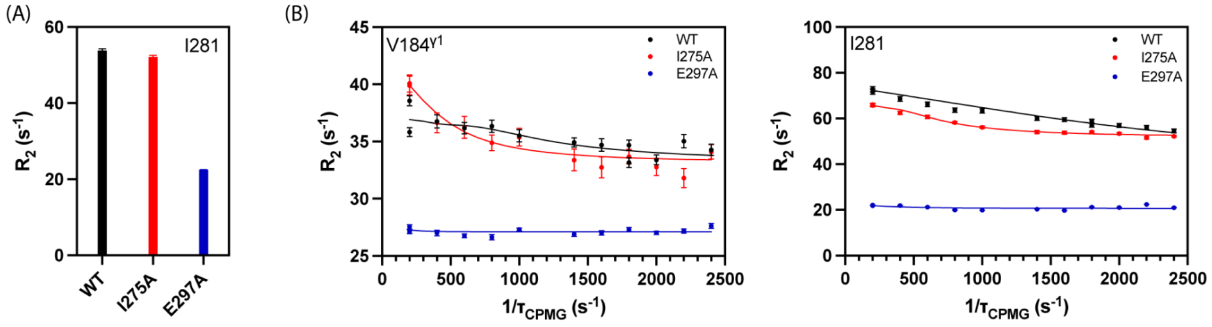

Figure 7. (A) Bar graph of the transverse relaxation rates of I281 in apo PTP1B at a τ_{cpmg} of 0.41667 ms at 800 MHz and 20 ms total relaxation time. (B) Carr−Purcell−Meiboom−Gill relaxation dispersion of apo PTP1B collected at 800 MHz with a total relaxation time of 20 ms showing V184$^{\gamma 1}$ and I281.

structural mediator. Thus, while both mutations perturb PTP1B dynamics, E297A exerts a more pronounced effect, consistent with its stronger impact on catalysis.

This trend extends to V184 within the acid loop, where ^{13}C relaxation dispersion profiles are similar for WT and I275A but flat for E297A, indicating a loss of millisecond-timescale motions for E297A (Figure 7). Complementary MD simulations also reveal rigidification of the acid loop on the faster nanosecond timescale, as reflected in negative ΔRMSF values (Figure 4). These dynamic changes propagate beyond

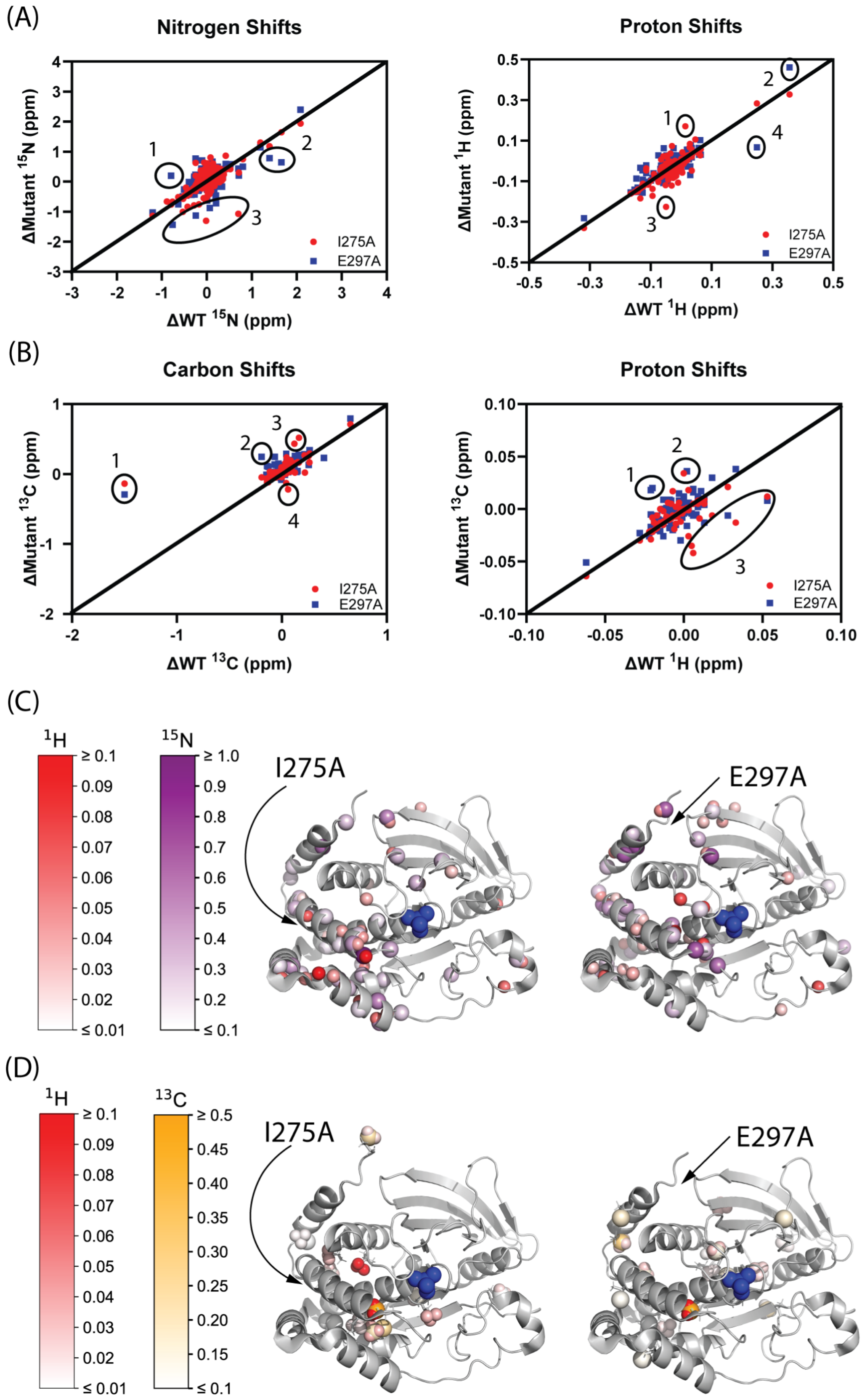

Figure 8. Correlation plots showing the vanadate-induced chemical shift changes comparing WT and mutant enzymes (I275A red, E297A blue). (A) $^{15}N^{H}$ (left) and $^{1}H^{N}$ (right) chemical shift changes (apo − bound). In each panel, residues with significant deviations from the diagonal, indicating mutant-specific differences in response to vanadate binding are circled. For $^{15}N^{H}$ (left), these residues are S80 (Group 1), L232, I261, T263, A264, W291, and D298 (Group 2), and G277 and G283 (Group 3). For $^{1}H^{N}$ (right), these residues are A264 (Group 1), G183 (Group 2), W16 (Group 3), and G283 (Group 4). (B) $^{13}C^{me}$ (left) and $^{1}H^{me}$ (right) chemical shift changes (apo − bound). In each panel, residues with significant deviations from the diagonal, indicating mutant-specific differences in response to vanadate binding are circled. For $^{13}C^{me}$ (left), these

Figure 8. continued

residues are I261 (Group 1), V287 (Group 2), and L250 and L299 (Groups 3 and 4). For $^{1}H^{me}$ (right), these residues are L110 and V155 (Group 1), L59 and V212 (Group 2), and L192, I219, L250, I281, and V287. The perpendicular distance between the data points and the diagonal was measured. Those values above 1.5 standard deviations from the 10% trimmed mean are mapped onto the crystal structure (PDB entry 3I80) in spheres with a color gradient in parts (C) and (D), where the VO_4^{3-} in the center is marked in blue. The sites of mutation are indicated with arrows.

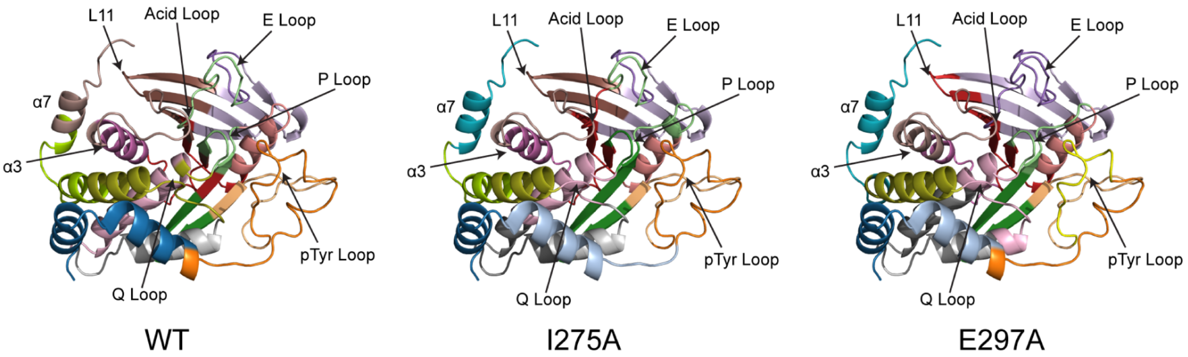

Figure 9. Allosteric communities derived from the generalized correlation coefficient from 1.6 μs of MD simulations. Communities are grouped by color. Note the change in the α7/acid loop community in WT in favor of the lone α7 community in I275A and E297A. E297A also shows a switch in the community to which the E-loop belongs, whereas the E-loop in I275A remains as it is in WT PTP1B.

the acid loop, influencing other elements of the active site. Further support comes from ^{13}C multiple-quantum methyl relaxation dispersion experiments, where E297A shows no dispersion in contrast to WT, underscoring a loss of conformational exchange in the acid loop of E297A on the millisecond timescale.

To further probe the impact of I275A and E297A on the PTP1B active site, we analyzed chemical shift changes upon binding of the transition-state analog vanadate (VO_4^{3-}).[62,63] A correlation plot of VO_4^{3-}-binding-induced methyl ^{13}C chemical shifts for WT, E297A, and I275A is shown in Figure 8 and SI Figure 6, with notable deviations highlighted. For I275A, affected residues include residues I261, L250, and L299. Importantly, I261 lies adjacent to Q262, the catalytic glutamine residue that orients a water molecule for the hydrolysis step during catalysis. The side chain of L250 is involved in direct hydrophobic packing with the side chain of I261, while L299 is located in α7, further highlighting the aforementioned coupled interactions between the active site and α7. In E297A, deviations also involve I261 along with I57, V113 (E-loop), V213 (P-loop), I275, I281, V287, and L294.

Analysis of the VO_4^{3-}-binding-induced methyl proton chemical shift changes (Figure 8B) revealed a similar set of affected residues for I275A, including L250, L192, L195, I219, and I281. Notably, I219 is located in the P-loop, while L192 is near the acid loop and packs against α6, suggesting that mutation at I275 perturbs ligand interactions at the active site. I281, positioned at the C-terminal end of α6, is also affected. For E297A, deviations were detected at L110 in the N-terminus of the E-loop, V155 in the "197" site,[29] and I281 in loop L18.

The correlation plot of ^{15}N-amide chemical shifts (Figure 8A) from VO_4^{3-} binding reveals additional perturbations in the protein backbone of the I275A and E297A variants. Affected residues include residues L232, A264, and K292. The connection between L232 in helix α4 and the acid loop has been reported previously, as this residue consistently exhibits perturbations upon mutations within the acid loop.[34] Similarly, residues near Q262, including A264, show clear chemical shift perturbations. K292, located in allosteric helix α7, also displays significant deviations relative to the wild type.

In the E297A variant, chemical shift deviations extend to multiple regions: S80 in β3, T177 in the acid loop, T263 in the Q-loop, and G283 in L18, as well as W291, K292, and D298 in α7. Notably, S80 lies within the 78−95 peptide segment, which undergoes enhanced amide exchange with deuterated buffer upon binding of the allosteric inhibitor BB3.[28]

Amide proton shift deviations (Figure 8A) further highlight structural disruptions in I275A, particularly in the N-terminal helices α1′ and α2′ (D11, W16). Additional effects are observed at A77 (immediately preceding β3), A264 (following the Q-loop), and A278 (within α6). For E297A, significant perturbations are detected in I10 (in α1′), A27 (after α2′), G183 and V184 (acid loop), A228, Q262, and V274 (in α6), and G283 (in L18).

Alteration of Allosteric Communities. We have investigated allosteric interactions in PTP1B using community network analysis derived from molecular dynamics simulations.[64,65] In WT PTP1B (Figure 9 and SI Figure 7), the acid loop and α7 helix cluster belong to the same community (light brown) and are dynamically coupled, consistent with prior reports.[27,29,31,35,42,61] In both E297A and I275A, however, this community splits: α7 forms an independent community, indicating the destabilization of α7 and the loss of coupling with the acid loop. Previous studies have shown that destabilization of α7 promotes the open (inactive) conformation of the acid loop.[27,29,31,42,61] Although the mutation sites are about 20 Å apart, E297A and I275A may affect PTP1B activity via a similar mechanism.

Differences emerge in the L11 community (dark brown), another key feature in the allosteric regulation of the acid loop dynamics. In WT PTP1B, the L11 community (dark brown) spans the central β-sheet adjacent to the acid loop, E-loop, and P-loop. β-sheets have been shown to facilitate long-range correlations in proteins, which could link L11 to these important loops.[66] In I275A, L11 is isolated from the β-sheet, while in E297A, L11 and the central β-sheet merge with the S-loop community (red), which is directly C-terminal to helix $\alpha3$. Both NMR and computational studies have implicated this region in modulating acid loop dynamics and PTP1B activity.[67−70] Thus, differences in the allosteric organization of L11 likely contribute to the distinct catalytic behavior of the two mutants.

Beyond these structural rearrangements, mutations also reshape the allosteric network governing substrate recognition. In particular, the pTyr loop community (orange in WT and I275A) splits into two communities in E297A. Since the pTyr loop harbors key residues for peptide binding, its dynamic decoupling from adjacent loops in E297A is likely to alter binding affinity. In WT PTP1B, the Q-loop and N-terminal region of $\alpha6$ belong to the same community (gold), which also includes G220 and I219 of the catalytic P-loop. By contrast, in both E297A and I275A, the Q-loop and these P-loop residues disengage from $\alpha6$ and instead couple with the C-terminal end of $\alpha4$ (light pink). Both $\alpha4$ and $\alpha6$ have been implicated in regulating PTP1B activity,[31,34,35,69] suggesting that altered connectivity between these elements (i.e., the Q-loop and P-loop) contributes to changes in activity and substrate recognition.

In WT PTP1B, the P-loop and E-loop belong to the same community (light green). However, in both E297A and I275A, the two loops separate into distinct communities. Prior work has shown that the E-loop is coordinated with the P-loop, and its motions are further correlated with the acid loop in WT PTP1B.[60,71] Furthermore, increased flexibility in the E-loop (Figure 4) has been suggested to influence both substrate binding and catalytic activity.[60] Altogether, the differential alterations in catalytically important loops—the acid loop, pTyr loop, Q-loop, P-loop, and E-loop—are likely to contribute to altered substrate specificity. To identify the most influential structural elements within the correlation network, we computed eigenvector centrality from the correlation coefficient matrix.[53] Eigenvector centrality can measure the strength of each residue's connectivity and communication in the correlation network, where a large eigenvector centrality represents a large influence on the network.[53] Previous computational studies using dynamic cross-correlation identified the acid loop and nearby regions, such as $\alpha3$, as displaying high eigenvector centrality.[71] Consistent with these findings, our analysis highlights high centrality for residues in the acid loop as well as in $\alpha7$ (SI Figure 8). Although $\alpha3$ residues exhibit low centrality in WT PTP1B, both E297A and I275A display the largest increases in centrality within $\alpha3$ and $\alpha7$ compared to WT. Prior studies have reported dynamic coupling between these helices, suggesting that they jointly regulate acid loop dynamics.[31,35,42,61] Despite evidence of $\alpha7$ destabilization in both mutants, its motions remain central to the PTP1B dynamics. Importantly, different communities exhibit distinct centrality changes across the mutants: I275A shows large increases in the $\alpha1'$ helix (dark blue), whereas E297A shows minimal changes in $\alpha1'$ but strong centrality increases in the Q-loop/P-loop community (light pink). These mutation-specific alterations in network centrality ultimately lead to differential substrate interactions and altered catalytic constants.

■ CONCLUSIONS

Enzymes exist as ensembles of conformations, each with distinct ligand-binding affinities and catalytic efficiencies. To rationalize the observed changes in kinetic parameters, we propose a kinetic model analogous to those described previously.[72,73] Our kinetic, computational, and NMR data indicate that $K_{i,1}$ is biased in WT to favor the E* state relative to I275A and E297A. This shift accounts for the primary effect of the mutants—reduced peptide K_m values compared to those of WT—summarized in Scheme 1.

Scheme 1. Kinetic Model for PTP1B Considering Alternate Conformations in Both apo and Substrate (Ligand)−Bound States

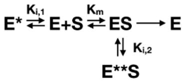

From Scheme 1, a Michaelis−Menten-like expression can be derived:

$$v = \frac{V_{\mathrm{m,eff}}[\mathrm{S}]}{K_{\mathrm{m,eff}}[\mathrm{S}]} \tag{3}$$

Here, the effective kinetic constants are modified by additional equilibria ($K_{i,1}$ and $K_{i,2}$). We propose that the mutations alter these equilibria, shifting the balance between more- and less-active and binding-competent versus incompetent ensembles. Moreover, the distinct effects on k_{cat} suggest that mutations differentially perturb $K_{i,2}$ in a substrate-dependent manner.

Accordingly, the effective parameters are

$$K_{\mathrm{m,eff}} = K_{\mathrm{m}}\frac{1 + (K_{i,1})^{-1}}{1 + (K_{i,2})^{-1}} \tag{4}$$

$$V_{\mathrm{m,eff}} = \frac{V_{\mathrm{m}}}{1 + (K_{i,2})^{-1}} \tag{5}$$

with inhibitory equilibrium constants defined as $K_{i,1} = [\mathrm{E}]/[\mathrm{E}^*]$ and $K_{i,2} = [\mathrm{ES}]/[(\mathrm{E}^{**}\mathrm{S})]$.

Overall, these findings demonstrate that allosteric mutations reshape the PTP1B energy landscape to regulate both substrate binding and catalysis. They further suggest that studies of enzyme allostery based on small-molecule substrates may not fully capture the cellular function of an enzyme compared to those of the more natural peptide substrates.

■ ASSOCIATED CONTENT

Supporting Information

The Supporting Information is available free of charge at https://pubs.acs.org/doi/10.1021/acs.biochem.5c00539.

SI Table 1: oligonucleotide sequences; SI Table 2: enzyme kinetic data; SI Table 3: NMR relaxation rates; SI Figure 1: enzyme reaction progress curves; SI Figure 2: fits to kinetic data from SI Figure 1; SI Figures 3−4: analysis of Molecular Dynamics simulations; SI Figure 5: NMR relaxation dispersion curves; SI Figure 6: NMR chemical shift perturbations; SI Figure 7: eigenvector analysis of WT and mutants (PDF)

Accession Codes

PTP1B, UniProtKB: P18031.

■ AUTHOR INFORMATION

Corresponding Authors

J. Patrick Loria − *Department of Chemistry, Yale University, New Haven, Connecticut 06511, United States; Department* *of Molecular Biophysics and Biochemistry, Yale University, New Haven, Connecticut 06520, United States;* orcid.org/0000-0002-4824-9089; Email: patrick.loria@yale.edu

Victor Batista – *Department of Chemistry, Yale University, New Haven, Connecticut 06511, United States;* orcid.org/0000-0002-3262-1237; Email: victor.batista@yale.edu

Authors

Xiaoyuan Wang – *Department of Chemistry, Yale University, New Haven, Connecticut 06511, United States*

Ryan M. Anderson – *Department of Chemistry, Yale University, New Haven, Connecticut 06511, United States;* orcid.org/0009-0004-9853-2458

Jinchan Liu – *Department of Chemistry, Yale University, New Haven, Connecticut 06511, United States;* orcid.org/0000-0003-2217-1233

Complete contact information is available at: https://pubs.acs.org/10.1021/acs.biochem.5c00539

Author Contributions

The manuscript was written through contributions of all authors. All authors have given approval to the final version of the manuscript.

Funding

J.P.L. acknowledges funding from NIH (R01 GM112781), V.S.B. acknowledges funding from the NSF (2412821), R.A. acknowledges that research was supported by the National Institute of General Medical Sciences of the National Institutes of Health (T32GM149438). The content is solely the responsibility of the authors and does not necessarily represent the official views of the National Institutes of Health. This material is based on work supported by the National Science Foundation Graduate Research Fellowship Program under Grant no (DGE-2139841) to R.A. Any opinions, findings, and conclusions or recommendations expressed in this material are those of the authors and do not necessarily reflect the views of the National Science Foundation.

Notes

The authors declare no competing financial interest.

REFERENCES

(1) Feldhammer, M.; Uetani, N.; Miranda-Saavedra, D.; Tremblay, M. L. PTP1B: A Simple Enzyme for a Complex World. *Crit. Rev. Biochem. Mol. Biol* **2013**, *48* (5), 430–445.

(2) Zhang, Z.-Y. Chemical and Mechanistic Approaches to the Study of Protein Tyrosine Phosphatases. *Acc. Chem. Res* **2003**, *36* (6), 385–392.

(3) Yu, Z.-H.; Zhang, Z.-Y. Regulatory Mechanisms and Novel Therapeutic Targeting Strategies for Protein Tyrosine Phosphatases. *Chem. Rev* **2018**, *118* (3), 1069–1091.

(4) Shen, R.; Crean, R. M.; Olsen, K. J.; Corbella, M.; Calixto, A. R.; Richan, T.; Brandao, T. A. S.; Berry, R. D.; Tolman, A.; Loria, J. P.; Johnson, S. J.; Kamerlin, S. C. L.; Hengge, A. C. Insights into the Importance of WPD-Loop Sequence for Activity and Structure in Protein Tyrosine Phosphatases. *Chem. Sci* **2022**, *13* (45), 13524–13540.

(5) Whittier, S. K.; Hengge, A. C.; Loria, J. P. Conformational Motions Regulate Phosphoryl Transfer in Related Protein Tyrosine Phosphatases. *Science* **2013**, *341* (6148), 899–903.

(6) Khajehpour, M.; Wu, L.; Liu, S.; Zhadin, N.; Zhang, Z. Y.; Callender, R. Loop Dynamics and Ligand Binding Kinetics in the Reaction Catalyzed by the Yersinia Protein Tyrosine Phosphatase. *Biochemistry* **2007**, *46* (14), 4370–4378.

(7) Zhang, Z. Y.; Maclean, D.; McNamara, D. J.; Sawyer, T. K.; Dixon, J. E. Protein Tyrosine Phosphatase Substrate Specificity: Size and Phosphotyrosine Positioning Requirements in Peptide Substrates. *Biochemistry* **1994**, *33* (8), 2285–2290.

(8) Zhang, Z. Y.; Thieme-Sefler, A. M.; Maclean, D.; McNamara, D. J.; Dobrusin, E. M.; Sawyer, T. K.; Dixon, J. E. Substrate Specificity of the Protein Tyrosine Phosphatases. *Proc. Natl. Acad. Sci. U. S. A* **1993**, *90* (10), 4446–4450.

(9) Sarmiento, M.; Zhao, Y.; Gordon, S. J.; Zhang, Z. Y. Molecular Basis for Substrate Specificity of Protein-Tyrosine Phosphatase 1B. *J. Biol. Chem* **1998**, *273* (41), 26368–26374.

(10) Tonks, N. K.; Neel, B. G. Combinatorial Control of the Specificity of Protein Tyrosine Phosphatases. *Curr. Opin. Cell Biol* **2001**, *13* (2), 182–195.

(11) Mertins, P.; Eberl, H. C.; Renkawitz, J.; Olsen, J. V.; Tremblay, M. L.; Mann, M.; Ullrich, A.; Daub, H. Investigation of Protein-Tyrosine Phosphatase 1B Function by Quantitative Proteomics. *Mol. Cell. Proteomics* **2008**, *7* (9), 1763–1777.

(12) Sarmiento, M.; Puius, Y. A.; Vetter, S. W.; Keng, Y.-F.; Wu, L.; Zhao, Y.; Lawrence, D. S.; Almo, S. C.; Zhang. Z.-Y. *Biochemistry* **2000**, *39* (28), 8171–8179.

(13) Ferrari, E.; Tinti, M.; Costa, S.; Corallino, S.; Nardozza, A. P.; Chatraryamontri, A.; Ceol, A.; Cesareni, G.; Castagnoli, L. Identification of New Substrates of the Protein-Tyrosine Phosphatase PTP1B by Bayesian Integration of Proteome Evidence. *J. Biol. Chem* **2011**, *286* (6), 4173–4185.

(14) Salmeen, A.; Andersen, J. N.; Myers, M. P.; Tonks, N. K.; Barford, D. Molecular Basis for the Dephosphorylation of the Activation Segment of the Insulin Receptor by Protein Tyrosine Phosphatase 1B. *Mol. Cell* **2000**, *6* (6), 1401–1412.

(15) Myers, M. P.; Andersen, J. N.; Cheng, A.; Tremblay, M. L.; Horvath, C. M.; Parisien, J.-P.; Salmeen, A.; Barford, D.; Tonks, N. K. TYK2 and JAK2 Are Substrates of Protein-Tyrosine Phosphatase 1B *. *J. Biol. Chem* **2001**, *276* (51), 47771–47774.

(16) Bakke, J.; Haj, F. G. Protein-Tyrosine Phosphatase 1B Substrates and Metabolic Regulation. *Semin. Cell. Dev. Biol* **2015**, *37*, 58–65.

(17) Ren, L.; Chen, X.; Luechapanichkul, R.; Selner, N. G.; Meyer, T. M.; Wavreille, A. S.; Chan, R.; Iorio, C.; Zhou, X.; Neel, B. G.; Pei, D. Substrate Specificity of Protein Tyrosine Phosphatases 1B, RPTPalpha, SHP-1, and SHP-2. *Biochemistry* **2011**, *50* (12), 2339–2356.

(18) Selner, N. G.; Luechapanichkul, R.; Chen, X.; Neel, B. G.; Zhang, Z.-Y.; Knapp, S.; Bell, C. E.; Pei, D. Diverse Levels of Sequence Selectivity and Catalytic Efficiency of Protein-Tyrosine Phosphatases. *Biochemistry* **2014**, *53* (2), 397–412.

(19) Denu, J. M.; Dixon, J. E. Protein Tyrosine Phosphatases: Mechanisms of Catalysis and Regulation. *Curr. Opin. Chem. Biol* **1998**, *2* (5), 633–641.

(20) Salmeen, A.; Barford, D. Functions and Mechanisms of Redox Regulation of Cysteine-Based Phosphatases. *Antioxid. Redox Signaling* **2005**, *7* (5–6), 560–577.

(21) Dadke, S.; Cotteret, S.; Yip, S. C.; Jaffer, Z. M.; Haj, F.; Ivanov, A.; Rauscher, F.; Shuai, K.; Ng, T.; Neel, B. G.; Chernoff, J. Regulation of Protein Tyrosine Phosphatase 1B by Sumoylation. *Nat. Cell Biol* **2007**, *9* (1), 80–85.

(22) Dadke, S.; Kusari, A.; Kusari, J. Phosphorylation and Activation of Protein Tyrosine Phosphatase (PTP) 1B by Insulin Receptor. *Mol. Cell. Biochem* **2001**, *221* (1), 147–154.

(23) Bandyopadhyay, D.; Kusari, A.; Kenner, K. A.; Liu, F.; Chernoff, J.; Gustafson, T. A.; Kusari, J. Protein-Tyrosine Phosphatase 1B Complexes with the Insulin Receptor in Vivo and Is Tyrosine-Phosphorylated in the Presence of Insulin. *J. Biol. Chem* **1997**, *272* (3), 1639–1645.

(24) Flint, A. J.; Gebbink, M. F.; Franza, B. R.; Hill, D. E.; Tonks, N. K. Multi-Site Phosphorylation of the Protein Tyrosine Phosphatase, PTP1B: Identification of Cell Cycle Regulated and Phorbol Ester Stimulated Sites of Phosphorylation. *EMBO J* **1993**, *12* (5), 1937–1946.

(25) Frangioni, J. V.; Beahm, P. H.; Shifrin, V.; Jost, C. A.; Neel, B. G. The Nontransmembrane Tyrosine Phosphatase PTP-1B Localizes to the Endoplasmic Reticulum via Its 35 Amino Acid C-Terminal Sequence. *Cell* **1992**, *68* (3), 545−560.

(26) Frangioni, J. V.; Oda, A.; Smith, M.; Salzman, E. W.; Neel, B. G. Calpain-Catalyzed Cleavage and Subcellular Relocation of Protein Phosphotyrosine Phosphatase 1B (PTP-1B) in Human Platelets. *EMBO J* **1993**, *12* (12), 4843−4856.

(27) Wiesmann, C.; Barr, K. J.; Kung, J.; Zhu, J.; Erlanson, D. A.; Shen, W.; Fahr, B. J.; Zhong, M.; Taylor, L.; Randal, M.; McDowell, R. S.; Hansen, S. K. Allosteric Inhibition of Protein Tyrosine Phosphatase 1B. *Nat. Struct. Mol. Biol* **2004**, *11* (8), 730−737.

(28) Woods, V. A.; Abzalimov, R. R.; Keedy, D. A. Native Dynamics and Allosteric Responses in PTP1B Probed by High-resolution HDX-MS. *Protein Sci* **2024**, *33* (6), No. e5024.

(29) Keedy, D. A.; Hill, Z. B.; Biel, J. T.; Kang, E.; Rettenmaier, T. J.; Brandao-Neto, J.; Pearce, N. M.; von Delft, F.; Wells, J. A.; Fraser, J. S. An Expanded Allosteric Network in PTP1B by Multitemperature Crystallography, Fragment Screening, and Covalent Tethering. *eLife* **2018**, *7*, No. e36307.

(30) Chartier, C. A.; Woods, V. A.; Xu, Y.; van Vlimmeren, A. E.; Johns, A. C.; Jovanovic, M.; McDermott, A. E.; Keedy, D. A.; Shah, N. H. Allosteric Regulation of the Tyrosine Phosphatase PTP1B by a Protein-Protein Interaction. *Protein Sci* **2025**, *34* (1), No. e70016.

(31) Choy, M. S.; Li, Y.; Machado, L. E. S. F.; Kunze, M. B. A.; Connors, C. R.; Wei, X.; Lindorff-Larsen, K.; Page, R.; Peti, W. Conformational Rigidity and Protein Dynamics at Distinct Timescales Regulate PTP1B Activity and Allostery. *Mol. Cell* **2017**, *65* (4), 644−658.e5.

(32) Montalibet, J.; Skorey, K.; McKay, D.; Scapin, G.; Asante-Appiah, E.; Kennedy, B. P. Residues Distant from the Active Site Influence Protein-Tyrosine Phosphatase 1B Inhibitor Binding*. *J. Biol. Chem* **2006**, *281* (8), 5258−5266.

(33) Xiao, P.; Wang, X.; Wang, H. M.; Fu, X. L.; Cui, F. A.; Yu, X.; Wen, S. S.; Bi, W. X.; Sun, J. P. The Second-Sphere Residue T263 Is Important for the Function and Catalytic Activity of PTP1B via Interaction with the WPD-Loop. *Int. J. Biochem. Cell Biol* **2014**, *57*, 84−95.

(34) Cui, D. S.; Beaumont, V.; Ginther, P. S.; Lipchock, J. M.; Loria, J. P. Leveraging Reciprocity to Identify and Characterize Unknown Allosteric Sites in Protein Tyrosine Phosphatases. *J. Mol. Biol* **2017**, *429* (15), 2360−2372.

(35) Cui, D.; Lipchock, J.; Brookner, D.; Loria, J. P. Uncovering the Molecular Interactions in the Catalytic Loop That Modulate the Conformational Dynamics in Protein Tyrosine Phosphatase 1B. *J. Am. Chem. Soc* **2019**, *141*, 12634−12647.

(36) Zhang, Z. Y. Kinetic and Mechanistic Characterization of a Mammalian Protein-Tyrosine Phosphatase, PTP1. *J. Biol. Chem* **1995**, *270* (19), 11199−11204.

(37) Zhang, Z. Y.; Maclean, D.; Thieme-Sefler, A. M.; Roeske, R. W.; Dixon, J. E. A Continuous Spectrophotometric and Fluorimetric Assay for Protein Tyrosine Phosphatase Using Phosphotyrosine-Containing Peptides. *Anal. Biochem* **1993**, *211* (1), 7−15.

(38) Goličnik, M. Exact and Approximate Solutions for the Decades-Old Michaelis-Menten Equation: Progress-Curve Analysis through Integrated Rate Equations. *Biochem. Mol. Biol. Educ* **2011**, *39* (2), 117−125.

(39) Goudar, C. T.; Sonnad, J. R.; Duggleby, R. G. Parameter Estimation Using a Direct Solution of the Integrated Michaelis-Menten Equation. *Biochim. Biophys. Acta, Protein Struct. Mol. Enzymol* **1999**, *1429* (2), 377−383.

(40) Tugarinov, V.; Sprangers, R.; Kay, L. E. Probing Side-Chain Dynamics in the Proteasome by Relaxation Violated Coherence Transfer NMR Spectroscopy. *J. Am. Chem. Soc* **2007**, *129* (6), 1743−1750.

(41) Meier, S.; Li, Y.-C.; Koehn, J.; Vlattas, I.; Wareing, J.; Jahnke, W.; Wennogle, L. P.; Grzesiek, S. Letter to the Editor: Backbone resonance assignment of the 298 amino acid catalytic domain of protein tyrosine phosphatase 1B (PTP1B). *J. Biomol. NMR* **2002**, *24* (2), 165−166.

(42) Torgeson, K. R.; Clarkson, M. W.; Kumar, G. S.; Page, R.; Peti, W. Cooperative Dynamics across Distinct Structural Elements Regulate PTP1B Activity. *J. Biol. Chem* **2020**, *295* (40), 13829−13837.

(43) Jorgensen, W. L.; Chandrasekhar, J.; Madura, J.; Impey, R.; Klein, M. Comparison of Simple Potential Functions for Simulating Liquid Water. *J. Chem. Phys* **1983**, *79* (2), 926−935.

(44) Phillips, J. C.; Braun, R.; Wang, W.; Gumbart, J.; Tajkhorshid, E.; Villa, E.; Chipot, C.; Skeel, R. D.; Kale, L.; Schulten, K. Scalable Molecular Dynamics with NAMD. *J. Comput. Chem* **2005**, *26* (16), 1781−1802.

(45) Huang, J.; MacKerell, A. D. CHARMM36 All-Atom Additive Protein Force Field: Validation Based on Comparison to NMR Data. *J. Comput. Chem* **2013**, *34* (25), 2135−2145.

(46) Martyna, G. J.; Tobias, D. J.; Klein, M. L. Constant Pressure Molecular Dynamics Algorithms. *J. Chem. Phys* **1994**, *101* (5), 4177−4189.

(47) Darden, T.; York, D.; Pedersen, L. Particle Mesh Ewald: An N-Log(N) Method for Ewald Sums in Large Systems. *J. Chem. Phys* **1993**, *98* (12), 10089−10092.

(48) Humphrey, W.; Dalke, A.; Schulten, K. VMD: Visual Molecular Dynamics. *J. Mol. Graphics* **1996**, *14* (1), 33−38.

(49) Maschietto, F.; Allen, B.; Kyro, G. W.; Batista, V. S. MDiGest: A Python Package for Describing Allostery from Molecular Dynamics Simulations. *J. Chem. Phys* **2023**, *158* (21), 215103.

(50) Michaud-Agrawal, N.; Denning, E. J.; Woolf, T. B.; Beckstein, O. MDAnalysis: A Toolkit for the Analysis of Molecular Dynamics Simulations. *J. Comput. Chem* **2011**, *32* (10), 2319−2327.

(51) Gowers, R. J.; Linke, M.; Barnoud, J.; Reddy, T. J. E.; Melo, M. N.; Seyler, S. L.; Domanski, J.; Dotson, D. L.; Buchoux, S.; Kenney, I. M., et al. *MDAnalysis: A Python Package for the Rapid Analysis of Molecular Dynamics Simulations*; Los Alamos National Laboratory (LANL: Los Alamos, NM, United States, 2019. .

(52) Schrodinger LLC. *The PyMOL Molecular Graphics System, Version 1.8*, Schrodinger LLC 2015.

(53) Negre, C. F. A.; Morzan, U. N.; Hendrickson, H. P.; Pal, R.; Lisi, G. P.; Loria, J. P.; Rivalta, I.; Ho, J.; Batista, V. S. Eigenvector Centrality for Characterization of Protein Allosteric Pathways. *Proc. Natl. Acad. Sci. U. S. A* **2018**, *115* (52), No. E12201−E12208.

(54) Lange, O. F.; Grubmuller, H. Generalized Correlation for Biomolecular Dynamics. *Proteins* **2006**, *62* (4), 1053−1061.

(55) Kraskov, A.; Stogbauer, H.; Grassberger, P. Estimating Mutual Information. *Phys. Rev. E: Stat., Nonlinear, Soft Matter Phys.* **2004**, *69* (6 Pt 2), 066138.

(56) Blondel, V. D.; Guillaume, J.-L.; Lambiotte, R.; Lefebvre, E. Fast Unfolding of Communities in Large Networks. *J. Stat. Mech* **2008**, *2008* (10), 10008.

(57) Hunter, J. D. Matplotlib: A 2D Graphics Environment. *Comput. Sci. Eng* **2007**, *9* (3), 90−95.

(58) *pandas-dev/pandas: Pandas*. Zenodo, 2025. .

(59) Harris, C. R.; Millman, K. J.; van der Walt, S. J.; Gommers, R.; Virtanen, P.; Cournapeau, D.; Wieser, E.; Taylor, J.; Berg, S.; Smith, N. J.; Kern, R.; Picus, M.; Hoyer, S.; van Kerkwijk, M. H.; Brett, M.; Haldane, A.; Del Río, J. F.; Wiebe, M.; Peterson, P.; Gérard-Marchant, P.; Sheppard, K.; Reddy, T.; Weckesser, W.; Abbasi, H.; Gohlke, C.; Oliphant, T. E. Array Programming with NumPy. *Nature* **2020**, *585* (7825), 357−362.

(60) Crean, R. M.; Biler, M.; van der Kamp, M. W.; Hengge, A. C.; Kamerlin, S. C. L. Loop Dynamics and Enzyme Catalysis in Protein Tyrosine Phosphatases. *J. Am. Chem. Soc* **2021**, *143* (10), 3830−3845.

(61) Olmez, E. O.; Alakent, B. Alpha7 Helix Plays an Important Role in the Conformational Stability of PTP1B. *J. Biomol. Struct. Dyn* **2011**, *28* (5), 675−693.

(62) Brandao, T. A.; Hengge, A. C.; Johnson, S. J. Insights into the Reaction of Protein-Tyrosine Phosphatase 1B: Crystal Structures for Transition State Analogs of Both Catalytic Steps. *J. Biol. Chem* **2010**, *285* (21), 15874−15883.

(63) Messmore, J. M.; Raines, R. T. Pentavalent Organo-Vanadates as Transition State Analogues for Phosphoryl Transfer Reactions. *J. Am. Chem. Soc* **2000**, *122*, 9911−9916.

(64) Sethi, A.; Eargle, J.; Black, A. A.; Luthey-Schulten, Z. Dynamical Networks in tRNA: Protein Complexes. *Proc. Natl. Acad. Sci. U. S. A* **2009**, *106* (16), 6620−6625.

(65) Rivalta, I.; Sultan, M. M.; Lee, N. S.; Manley, G. A.; Loria, J. P.; Batista, V. S. Allosteric Pathways in Imidazole Glycerol Phosphate Synthase. *Proc. Natl. Acad. Sci. U. S. A* **2012**, *109* (22), No. E1428−36.

(66) Fenwick, R. B.; Orellana, L.; Esteban-Martín, S.; Orozco, M.; Salvatella, X. Correlated Motions Are a Fundamental Property of *β*-Sheets. *Nat. Commun* **2014**, *5* (1), 4070.

(67) Kamerlin, S. C. L.; Rucker, R.; Boresch, S. A Targeted Molecular Dynamics Study of WPD Loop Movement in PTP1B. *Biochem. Biophys. Res. Commun* **2006**, *345* (3), 1161−1166.

(68) Kamerlin, S. C. L.; Rucker, R.; Boresch, S. A Molecular Dynamics Study of WPD-Loop Flexibility in PTP1B. *Biochem. Biophys. Res. Commun* **2007**, *356* (4), 1011−1016.

(69) Torgeson, K. R.; Clarkson, M. W.; Granata, D.; Lindorff-Larsen, K.; Page, R.; Peti, W. Conserved Conformational Dynamics Determine Enzyme Activity. *Sci. Adv* **2022**, *8* (31), No. eabo5546.

(70) Peters, G. H.; Frimurer, T. M.; Andersen, J. N.; Olsen, O. H. Molecular Dynamics Simulations of Protein-Tyrosine Phosphatase 1B. I. Ligand-Induced Changes in the Protein Motions. *Biophys. J* **1999**, *77* (1), 505−515.

(71) Welsh, C. L.; Madan, L. K. Protein Tyrosine Phosphatase Regulation by Reactive Oxygen Species. *Adv. Cancer Res* **2024**, *162*, 45−74.

(72) Butterwick, J. A.; Loria, J. P.; Astrof, N. S.; Kroenke, C. D.; Cole, R.; Rance, M.; Palmer, A. G. Multiple Time Scale Backbone Dynamics of Homologous Thermophilic and Mesophilic Ribonuclease HI Enzymes. *J. Mol. Biol* **2004**, *339* (4), 855−871.

(73) Kempf, J. G.; Jung, J.; Ragain, C.; Sampson, N. S.; Loria, J. P. Dynamic Requirements for a Functional Protein Hinge. *J. Mol. Biol* **2007**, *368* (1), 131−149.